Supplementary Materials for

Inverse topological insulator with tunable intersurface coupling

Matthew Brahlek[1†], Nikesh Koirala[1†], Jianpeng Liu[1], Tahir I. Yusufaly[1], Maryam Salehi[2], Myung-Geun Han[3], Yimei Zhu[3], David Vanderbilt[1], and Seongshik Oh[1,*]

[1]Department of Physics & Astronomy, Rutgers, The State University of New Jersey, Piscataway, New Jersey 08854, U.S.A.

[2]Department of Materials Science and Engineering, Rutgers, The State University of New Jersey, Piscataway, New Jersey 08854, U.S.A.

[3]Condensed Matter Physics & Materials Science, Brookhaven National Lab, Upton, NY 11973, U.S.A.

*Correspondence should be addressed to ohsean@physics.rutgers.edu

[†]These authors contributed equally to this work

Contents:

A: Experimental methods

All samples were grown using 10 mm × 10 mm *c*-plane Al_2O_3 substrates. The first Bi_2Se_3 layer was grown according to the two-step growth method developed at Rutgers University where the first 3 QL was grown at 135°C, which was followed by slowly annealing the sample to 300°C, where the subsequent 27 QL of Bi_2Se_3 layers were grown. Once the first Bi_2Se_3 layer finished growth, the In_2Se_3 of the specified thickness was grown, followed by the remaining Bi_2Se_3 layer. All the samples were then capped by 50 QL of In_2Se_3 which stabilized the films during exposure to atmosphere. For the samples with $(Bi_{1-x}In_x)_2Se_3$ as the barrier layer, the same basic recipe was used. The Bi and In cell temperatures were adjusted such that when opened together the resulting film gave the concentration that was sought. All the concentrations were checked by a combination of ex situ Rutherford back scattering spectroscopy and in situ quartz crystal microbalance measurements, and the results were within ±1% of the target values.

All transport measurements were carried out at 1.5 K using the standard Van der Pauw lead geometry, and the magnetic field was applied perpendicular to the films' surface. The raw data was symmetrized to remove any odd component from R_{xx} and any even component from R_{xy}. The carrier density and mobility of the films ranged between 3-7 × 10^{13} /cm^2 and 500-1000 cm^2/Vs, and there was no correlation between the transport data and the value of $\tilde{A}$. From the WAL fitting, l_ϕ ranged between 50-100 nm and also showed little correlation with the other transport data or $\tilde{A}$. The temperature dependence of resistivity for all samples showed typical monotonic decreasing behavior with decreasing temperature, which is typical of a metal. $\tilde{A}$ was independent of temperature below ~20 K, above which deviation occurred as thermal effect suppresses the WAL signal.

TEM sample preparation was carried out with focused-ion beam (FIB) technique using 5 keV Ga^+ ions. A JEOL ARM 200CF equipped with a cold field-emission gun and double-spherical aberration correctors operated at 200 kV was used for high-angle annular dark-field (HAADF) scanning transmission electron microscopy (STEM) with the collection angles ranging from 68 to 280 mrad.

B: Computational methods

B1. Tunneling between topological interface states

We study the tunneling between the topological surface states (TSS) in Bi_2Se_3-In_2Se_3-Bi_2Se_3 heterostructures based on density-functional theory (DFT) (1-2). We first use the Quantum ESPRESSO package (3) to perform calculations on bulk Bi_2Se_3 and In_2Se_3, with the generalized gradient approximation (GGA) (4) to the exchange-correlation functional and fully relativistic norm-conserving pseudopotentials. The Brillouin zone (BZ) is sampled on an 8×8×8 Monkhorst-Pack (5) k mesh, with an energy cutoff of 55 Ry (1 Ry ≈ 13.6 eV) for Bi_2Se_3 and 65 Ry for In_2Se_3. The first-principles output is fed into the Wannier90 package to produce Wannier functions (WFs) and to generate a realistic tight-binding (TB) model defined in the chosen Wannier basis (*6-7*). 30 Wannier functions are constructed for Bi_2Se_3, including all the valence p orbitals, while four extra In 5s orbitals are included for In_2Se_3. Both models are constructed in such a way that they exactly reproduce the first-principles bandstructures within a certain energy range, spanning from 3 eV below to 3 eV above the Fermi level.

Once the first-principles TB model is obtained, we are ready to construct supercells including a Bi_2Se_3-In_2Se_3 interface. First, the Wannier-based model Hamiltonians for bulk Bi_2Se_3 and In_2Se_3, denoted as H_1 and H_2, are extrapolated to N_1 QL and N_2 QL slabs stacked in the [111] direction with open boundary conditions. These two isolated slabs are connected together in such a way that all the first-neighbor hoppings (by first-neighbor hopping, we actually refer to hopping terms between nearest-neighbor QLs) across the interface are taken as the average value of the corresponding hopping terms in the Bi_2Se_3 and In_2Se_3 bulk TB models. Then the periodic boundary condition is applied to the (N_1 + N_2)-QL slab to make it a periodic supercell. In our calculations, the total thickness of Bi_2Se_3 and In_2Se_3 is fixed to be N_1 + N_2 = 12 QLs, and the thickness of In_2Se_3 is varied from N_2 = 1 to 6 QLs (for the data shown in Fig. 2 H of the main text, N_1 + N_2 = 16 QLs with N_2 = 8). Working in the Wannier basis allows for the thickness of In_2Se_3 in the heterostructure to be highly tunable, and the computational cost is negligible compared with a fully self-consistent interface calculation.

In implementing this procedure, two issues need to be addressed. First, at the bulk level, we note that standard DFT tends to underestimate the energy of the In 5*s* level. Because the lowest conduction band and highest valence band of In_2Se_3 are dominated by In 5*s* and Se 4*p* orbitals respectively, DFT predicts a smaller band gap compared with experiment (8). Here we adopt the corrective treatment described in Ref. (8) which involves applying a +0.79 eV rigid shift (taken from many-body GW calculations) to the four In 5*s* levels in the 34-band model for In_2Se_3, leaving all the other matrix elements unchanged.

Second, when constructing interface models, we have to take extra care of the band offset between the two bulk materials. Initially the zeroes of energy of the Wannierized tight-binding models for Bi_2Se_3 and In_2Se_3 are inherited from the respective bulk DFT bulk calculations, but as is well known, these are largely arbitrary, as they depend on irrelevant details such as the choice of pseudopotentials. We adopt the alignment method based on surface work functions (9) by carrying out self-consistent surface slab calculations on Bi_2Se_3 and In_2Se_3 slabs individually, from which we evaluate the difference between the average electrostatic potential energy deep in the bulk vs in the vacuum for each material. We do this by computing the macroscopic-averaged electrostatic potential $\overline{V}(z)$ from the microscopic potential $V(x,y,z)$ as: $\overline{V}(z) = (cA)^{-1} \int_{z-c/2}^{z+c/2} dz \iint_A dxdy\, V(x,y,z)$, where c and A are the cell height (size of a QL) and basal area respectively. For these calculations, a 3-QL slab is used, and slabs are separated from each other by a vacuum space of 2.9 nm. The macroscopic averages of the electrostatic potentials are plotted in Fig. S1. Note that due to the non-polar crystal structure and the homogeneous nature of the vacuum, $\overline{V}(z)$ remains constant both deep in the bulk and in vacuum. Aligning the vacuum levels, we conclude that the relative shift between the average electrostatic potential in bulk Bi_2Se_3 vs In_2Se_3 is $\Delta V = V_2 - V_1 = 1.776$ eV. Therefore, the arbitrariness in the energy zeroes can be removed by shifting all the Kohn-Sham eigenenergies of In_2Se_3 using $\tilde{E}_n(\mathbf{k}) = E_n(\mathbf{k}) + \Delta V$.

With the GW correction to In 5*s* levels and the shift ΔV on all the In_2Se_3 on-site energies, our interface model is ready to be used for the superlattice calculations. The eigenvalues are calculated in the

(k_x, k_y) plane, setting k_z = 0. If the TSS do not interact, we expect to see a doubly degenerate gapless Dirac cone around Γ (k_x = 0, k_y = 0), but the energy spectrum should become gapped when a tunneling interaction is allowed. Therefore, the band gap at Γ, denoted as $\Delta(\Gamma)$, should provide a measure reflecting the tunneling amplitude between the TSSs. As shown in Fig. 2D in the main text, $\Delta(\Gamma)$ is found to drop exponentially as the thickness of the In_2Se_3 layer increases. Setting 0.05 eV as a threshold below which the tunneling between the TSS is considered as negligible, the corresponding critical thickness t_c is about ~2.6 QLs, which agrees well with experimental data.

One may also be interested in the real-space distribution of the interface states, which can be easily calculated using the interface model described above. We define the following quantity as a weight of the real space density of the interface states around the Fermi level (*10*): $\xi(z) = \sqrt{|\psi_\Gamma^v(z)|^2 + |\psi_\Gamma^c(z)|^2}$, where $\psi_\Gamma^v(z)$ and $\psi_\Gamma^c(z)$ are the components of the Bloch states at Γ projected onto the Wannier functions centered at z, and the superscripts v and c refer to the highest occupied and lowest unoccupied states respectively. In other words, if the Fermi level lies slightly above the conduction band minimum (CBM) at Γ, $\xi(z)^2$ measures the z-dependence of the charge density averaged over the x-y plane around the Fermi level. $\xi(z)$ is denoted as the real space density of the states (RDOS) in the main text, as shown in Fig. 2E-H.

B2. Band alignment

From the above self-consistent superlattice calculations, we are also able to determine the position of the In_2Se_3 conduction band minimum (CBM) and valence band maximum (VBM) with respect to the Bi_2Se_3 VBM. It turns out that the In_2Se_3 CBM and VBM at Γ (including the +0.79 eV correction on In 5*s* levels) are 1.286 eV above and -0.018 eV below the Bi_2Se_3 VBM respectively. Such information is useful in evaluating the band alignment in $(Bi_{1-x}In_x)_2Se_3$. However, if one tries to estimate the CBM and VBM positions for different x values simply by linearly interpolating the two end points (x = 0% and 100%), one would not get a reasonable result. Because a linear gap-closure picture does not apply to $(Bi_{1-x}In_x)_2Se_3$

over the entire x interval, the bulk band gap vanishes at very low In composition as a result of the In clustering tendency and the presence of In 5*s* orbitals (8) (*11*) (*12*). Therefore, in order to treat the band alignment in $(Bi_{1-x}In_x)_2Se_3$ better, we also extract the position of the 3D Dirac point at criticality from Ref. (8) which is 0.106 eV above the VBM of Bi_2Se_3. Even though the theoretical critical point of $(Bi_{1-x}In_x)_2Se_3$ ($x_c \approx 16.7\%$) is higher than the experimental value ($x_c \sim 6\%$, (*11*) $x_c \sim 4\% - 7\%$, (*12*)), here we assume that the theoretical shift of the 3D Dirac point with respect to the Bi_2Se_3 VBM at criticality also applies to the experimental situation. Namely, we assume that the 3D Dirac point is 0.106 eV above the Bi_2Se_3 VBM at $x = 6\%$.

Table S1: Band alignment of $(Bi_{1-x}In_x)_2Se_3$

x	0	6%	20%	60%	100%
VBM (eV)	0	0.106	0.088	0.035	−0.018
CBM (eV)	0.490	0.106	0.280	0.786	1.286

Using the positions of the CBM and VBM at 3 different x values as specified above (x = 0%, 6% and 100%), we can obtain the CBM and VBM for any other x from two separate linear interpolations in the left and right intervals partitioned by x_c. Under such an approximation, the gap vs x consists of two linear curves with different slopes, as shown in Fig. S2, instead of a single straight line as predicted by a simple linear-gap-closure picture.

Table S1 shows the alignments of the CBM and VBM of $(Bi_{1-x}In_x)_2Se_3$ with respect to the VBM of Bi_2Se_3 at different x. When x is 20%, the CBM of $(Bi_{1-x}In_x)_2Se_3$ is below that of Bi_2Se_3, which means that in a realistic case in which the Fermi level is slightly above the CBM of Bi_2Se_3, the $(Bi_{1-x}In_x)_2Se_3$ barrier layer would behave as a metal with the TSS extending through the entire barrier layer. On the other hand, the CBM goes above the Bi_2Se_3 CBM when x is 60%, such that the $(Bi_{1-x}In_x)_2Se_3$ layer acts as an actual potential barrier which would decouple the two TSS.

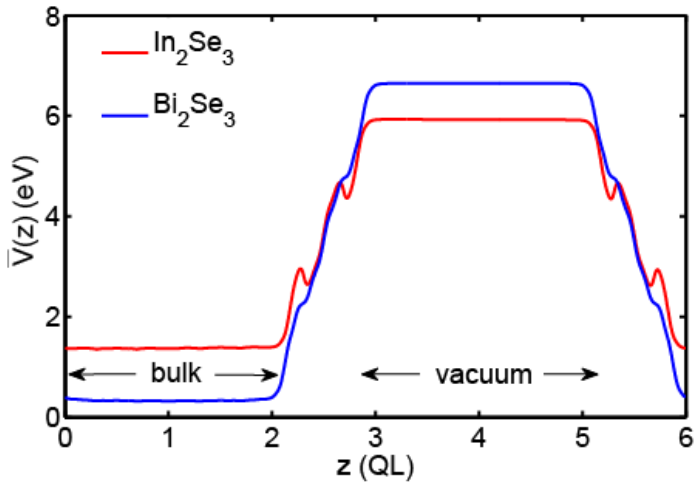

Fig. S1 The macroscopic average of the electrostatic potentials of Bi_2Se_3 and In_2Se_3 slabs.

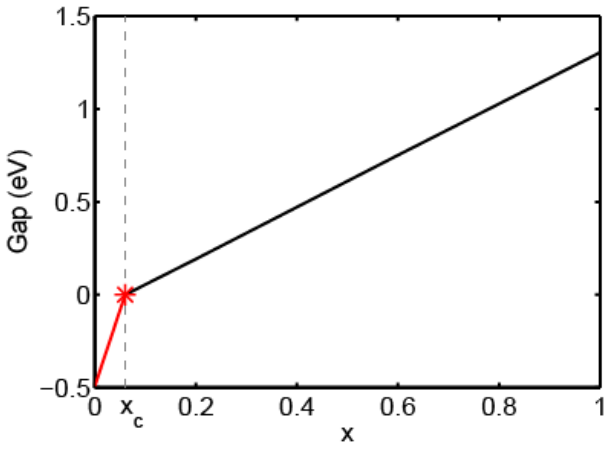

Fig. S2 The bulk gap of $(Bi_{1-x}In_x)_2Se_3$ at Γ from linear interpolations. The asterisk marks the critical point. A negative gap (red segment) indicates a topological band inversion.

References

1. P. Hohenberg, W. Kohn, *Phys. Rev.* **136**, B864 (1964).
2. W. Kohn, L. J. Sham, *Phys. Rev.* **140**, A1133 (1965).
3. P. Giannozzi *et al.*, *J. Phys. Cond. Matt.* **21**, 395502 (2009).
4. J. P. Perdew, K. Burke, M. Ernzerhof, *Phys. Rev. Lett.* **77**, 3865 (1996).
5. H. J. Monkhorst, J. D. Pack, *Phys. Rev. B* **13**, 5188 (1976).
6. N. Marzari, A. A. Mostofi, J. R. Yates, I. Souza, D. Vanderbilt, *Rev. Mod. Phys.* **84**, 1419 (2012).
7. A. A. Mostofi *et al.*, *Comp. Phys. Commun.***178**, 685 (2008).
8. J. Liu, D. Vanderbilt, *Phys. Rev. B* **88**, 224202 (2013).
9. N. E. Singh-Miller, N. Marzari, *Phys. Rev. B* **80**, 235407 (2009).
10. Q. Zhang, Z. Zhang, Z. Zhu, U. Schwingenschlögl, Y. Cui, *ACS Nano* **6**, 2345 (2012).
11. L. Wu *et al.*, *Nat. Phys.* **9**, 410 (2013).
12. M. Brahlek *et al.*, *Phys. Rev. Lett.***109**, 186403 (2012).